



Evidence for a spinon Kondo effect in cobalt atoms on single-layer 1T-TaSe₂

Yi Chen^{1,2,3,4,16}, Wen-Yu He[⊕]^{5,6,16}, Wei Ruan^{1,2,7,16}, Jinwoong Hwang^{8,9,10}, Shujie Tang^{8,9,11,12}, Ryan L. Lee^{1,13}, Meng Wu[⊕]^{1,2}, Tiancong Zhu^{1,2}, Canxun Zhang[⊕]^{1,2,14}, Hyejin Ryu^{8,15}, Feng Wang[⊕]^{1,2,14}, Steven G. Louie[⊕]^{1,2}, Zhi-Xun Shen[⊕]^{9,11}, Sung-Kwan Mo[⊕]⁸, Patrick A. Lee⁵ and Michael F. Crommie[⊕]^{1,2,14} ⋈

Quantum spin liquids are highly entangled, disordered magnetic states that are expected to arise in frustrated Mott insulators and to exhibit exotic fractional excitations such as spinons and chargons. Despite being electrical insulators, some quantum spin liquids are predicted to exhibit gapless itinerant spinons that yield metallic behaviour in the charge-neutral spin channel. We deposited isolated magnetic atoms onto single-layer 1T-TaSe₂, a candidate gapless spin liquid, to probe how itinerant spinons couple to impurity spin centres. Using scanning tunnelling spectroscopy, we observe the emergence of new, impurity-induced resonance peaks at the 1T-TaSe₂ Hubbard band edges when cobalt adatoms are positioned to have maximal spatial overlap with the local charge distribution. These resonance peaks disappear when the spatial overlap is reduced or when the magnetic impurities are replaced with nonmagnetic impurities. Theoretical simulations of a modified Anderson impurity model show that the observed peaks are consistent with a Kondo resonance induced by spinons combined with spin-charge binding effects that arise due to fluctuations of an emergent gauge field.

apless quantum spin liquids (QSLs) are predicted to act like 'neutral metals' that exhibit metallic behaviour in the spin channel despite being Mott insulators¹⁻⁹. Evidence for this exotic metal-like behaviour has been observed using thermal and magnetic measurements for several gapless QSL candidates¹⁰⁻¹³. These bulk probes, however, average over impurities and disorder, leading to inconsistent results for different samples 10,14-16 and/or alternative explanations for the experimental signatures¹⁷. Local probe measurements, on the other hand, allow direct comparison of defect-free regions of a material with regions containing well-defined impurities^{18,19}. Local magnetic moments are a particularly interesting type of impurity because their direct interactions with spinons allow them to potentially probe the effects of spinon itinerancy²⁰. In a conventional metal, the impurity moment is collectively screened by itinerant conduction electrons via the Kondo effect²¹. For a gapless QSL with a spinon Fermi surface, it has been predicted that itinerant spinons might also perform Kondo screening of magnetic impurities, yielding Kondo temperatures that scale similar to the conventional metallic case²⁰. Some experimental evidence for spinon Kondo screening has been obtained from muon spin rotation studies of the QSL candidate Zn-brochantite (ZnCu₃(OH)₆SO₄) that show reduced magnetic moments arising from Cu-Zn intersite disorder²². Local measurements of individual Kondo impurities in a QSL, however, have not yet been reported.

Here, we demonstrate the use of scanning tunnelling microscopy/spectroscopy (STM/STS) to probe the Kondo response of individual magnetic impurities in a gapless QSL. This measurement is complicated by the fact that QSLs are typically good insulators whereas STM requires a nonzero electrical conductivity to function. We have overcome this challenge by using a new two-dimensional gapless QSL candidate, single-layer (SL) 1T-TaSe2, that is supported by a sheet of conductive graphene and so allows injected charge to be drained away^{23,24}. STM imaging allows us to identify defect-free patches of SL 1T-TaSe, where we have previously discovered long-wavelength spatial modulations indicative of a half-filled spinon Fermi surface²⁴. In this work, we introduce individual magnetic impurities onto the clean 1T-TaSe, surface by vacuum deposition of a low coverage of Co atoms. By using STS at $T=5\,\mathrm{K}$, we observe that Co atoms having maximal spatial overlap with the 1T-TaSe₂ d-orbital charge distribution exhibit new resonance peaks at both the upper and lower Hubbard band edges in the vicinity of Co impurities. Nonmagnetic Au atoms deposited onto the 1T-TaSe, surface do not show this unusual behaviour. To understand why Co atoms on SL 1T-TaSe₂ generate new electron-hole band-edge resonances, we simulated our magnetic impurity system utilizing a modified Anderson model. Strong interaction effects were accounted for both in the substrate and in the impurity through a slave-rotor mean-field theory approach employing a U(1) gapless

Department of Physics, University of California, Berkeley, CA, USA. ²Materials Sciences Division, Lawrence Berkeley National Laboratory, Berkeley, CA, USA. ³International Center for Quantum Materials, School of Physics, Peking University, Beijing, China. ⁴Collaborative Innovation Center of Quantum Matter, Beijing, China. ⁵Department of Physics, Massachusetts Institute of Technology, Cambridge, MA, USA. ⁶School of Physical Science and Technology, ShanghaiTech University, Shanghai, China. ⁷State Key Laboratory of Surface Physics and Department of Physics, Fudan University, Shanghai, China. ⁸Advanced Light Source, Lawrence Berkeley National Laboratory, Berkeley, CA, USA. ⁹Stanford Institute for Materials and Energy Sciences, SLAC National Accelerator Laboratory and Stanford University, Menlo Park, CA, USA. ¹⁰Department of Physics, Kangwon National University, Chuncheon, Korea. ¹¹Geballe Laboratory for Advanced Materials, Departments of Physics and Applied Physics, Stanford University, Stanford, CA, USA. ¹²CAS Center for Excellence in Superconducting Electronics, Shanghai Institute of Microsystem and Information Technology, Chinese Academy of Sciences, Shanghai, China. ¹³Joseph Henry Laboratories and Department of Physics, Princeton University, Princeton, NJ, USA. ¹⁴Kavli Energy Nano Sciences Institute, University of California Berkeley and the Lawrence Berkeley National Laboratory, Berkeley, CA, USA. ¹⁵Center for Spintronics, Korea Institute of Science and Technology, Seoul, Korea. ¹⁶These authors contributed equally: Yi Chen, Wen-Yu He, Wei Ruan. ¹⁸Center for Spintronics, Korea Institute of Science and Technology, Seoul,

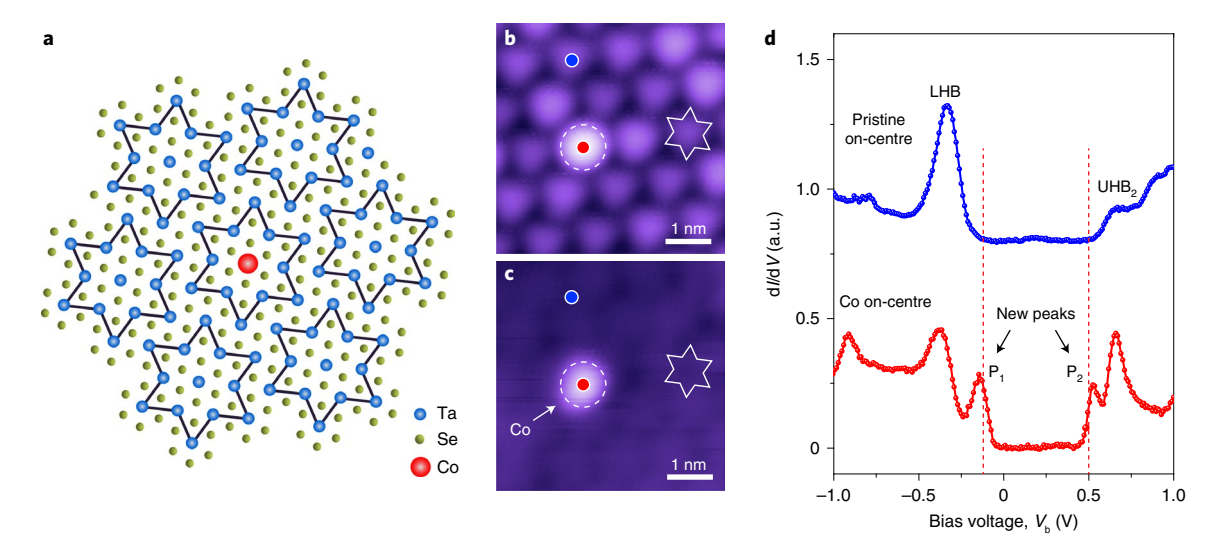


Fig. 1 | Co adatoms at the on-centre position on single-layer (SL) 1T-TaSe₂ show new resonance peaks at Hubbard band edges. **a**, The 1T-TaSe₂ structure, including the SOD CDW and on-centre Co adatom position. **b**, STM topograph acquired at moderate negative sample bias voltage, showing the Co adatom (dashed white line) as well as the SOD CDW superlattice (solid white line) for SL 1T-TaSe₂ ($V_b = -0.5 \text{ V}$, $I_t = 10 \text{ pA}$). **c**, STM topograph of the same area as **b** but acquired at high positive sample bias voltage, showing only the Co adatom (dashed white circle) ($V_b = 1.5 \text{ V}$, $I_t = 10 \text{ pA}$). Comparison of **b** and **c** confirms that the Co adatom is 'on-centre' (that is, located at the centre of the underlying CDW cell). **d**, Pristine SL 1T-TaSe₂ STM dl/dV spectrum (blue curve) obtained at the on-centre position of a CDW unit cell (blue dot in **b** and **c**). Features corresponding to the Hubbard bands are marked as LHB and UHB₂. dl/dV spectrum of a single Co adatom (red curve) in the on-centre position on SL 1T-TaSe₂ (red dot in **b** and **c**). Two new resonance peaks (labelled P_1 and P_2) appear near the Hubbard band edges (dashed lines) for on-centre Co ($V_b = -1 \text{ V}$, $I_t = 20 \text{ pA}$, $V_{rms} = 20 \text{ mV}$).

QSL. Our calculations show that the experimentally observed resonance peaks are consistent with the formation of a Kondo screening cloud in the QSL spin channel that can induce detectable band-edge resonances through emergent gauge-field fluctuations.

The main experimental result reported here was obtained for individual magnetic Co atoms positioned at the centre of the 1T-TaSe_2 charge density wave (CDW) unit cell. Magnetism in Co adatoms for this configuration is supported by density functional theory (DFT) simulations (Methods and Supplementary Fig. 1). As sketched in Fig. 1a, in the CDW phase of 1T-TaSe_2 , the Ta atom lattice distorts (due to electron–phonon interactions²⁵) to form a triangular superlattice of star-of-David (SOD) clusters, each composed of 13 Ta atoms. An STM image of a single Co atom sitting at the centre of a SOD cluster can be seen in the STM topograph of Fig. 1b (obtained at a sample bias voltage of $V_b = -0.5 \, \text{V}$). At this bias voltage, the SOD CDW superlattice can clearly be seen, and the Co adatom creates a bright protrusion ~1.4 Å high. Imaging the same region at a high positive bias of $V_b = 1.5 \, \text{V}$ reduces the CDW contrast, allowing the position of the Co atom to be determined more clearly (Fig. 1c).

An STS dI/dV spectrum obtained for a single Co atom on 1T-TaSe, is shown in Fig. 1d. Here, the blue curve shows the spectrum obtained when the STM tip is held over the centre of a pristine SOD cluster with no Co adatom (Fig. 1b,c, blue dot). Two peaks are seen, marking the lower Hubbard band (LHB) at $V_b = -0.34 \,\mathrm{V}$ and the upper Hubbard band (UHB₂) at $V_b = 0.62 \,\mathrm{V}$ for pristine SL 1T-TaSe₂, in agreement with previous results²³. The upper Hubbard band is marked 'UHB2' because another Hubbard band feature (UHB_1) occurs at lower energy $(V_b = 0.17 \text{ V})$ but with little weight (that is, reduced local density of states (LDOS)) at the SOD centre (Fig. 2b and ref. 23). The red curve shows the dI/dV spectrum measured while placing the STM tip above the Co atom shown in Fig. 1b,c (red dot). Two outer peaks are seen, corresponding to the LHB and UHB, features of the pristine surface. Strikingly, however, two new peaks are observed at $V_b = -0.15 \,\mathrm{V}$ (labelled P₁, just below the LHB band edge) and at $V_b = 0.53 \,\mathrm{V}$ (labelled P_2 , just above the UHB₂ band edge) (Supplementary Fig. 3). These two peaks are the main experimental finding of this paper. The P_1 and P_2 peaks are relatively narrow with a full-width at half-maximum of 106 and 90 meV, respectively.

The Co electronic structure is sensitive to where on the surface the adatom sits (Fig. 2). Here, local electronic structure variation can be seen in both our pristine surface spectroscopy and our 'on-Co' spectroscopy, depending on atomic position. In general there are three types of positions that Co atoms can occupy (Fig. 2a, sketch): (1) on-centre, (2) off-centre and (3) midway (with respect to the centre of a SOD unit cell). Co atoms occupying these three different positions can be seen in the topographs of Fig. 2c,d. One of the main differences between the three different positions is the strength of the pristine SL 1T-TaSe, Hubbard band LDOS (Fig. 2b). As shown previously²³, both the LHB and UHB₂ features exhibit high LDOS at the on-centre position but decrease monotonically as one moves outwards. The UHB₁ feature, in contrast, peaks at locations away from the SOD centre. This behaviour is reflected in the pristine (that is, off-Co) dI/dV spectra, which show the UHB₁ feature absent at the on-centre position but appearing more strongly for the off-centre or midway position (Fig. 2e, blue curves).

The on-Co dI/dV spectra in Fig. 2e (red curves) differ substantially when the Co atom sits at different positions. While the P₁ and P₂ features appear strongly for the on-centre position, they are completely absent when Co atoms occupy either the off-centre or midway position. At the off-centre position, Co atoms exhibit features that correspond to the LHB, UHB₁ and UHB₂ features, but the UHB₁ peak observed at $V_b = 0.25 \,\text{V}$ is slightly offset from the pristine UHB₁ feature at V_b = 0.17 V. At the midway position, Co atoms exhibit features corresponding to LHB and UHB2, but show no features corresponding to UHB₁. All of the spectroscopic features shown in Fig. 2c-e were reversibly reproduced when we shifted individual Co atoms from one position to another for all three positions using atom manipulation (Supplementary Figs. 4, 5 and Note 3). This helps to clarify that the spectroscopic features highlighted above arise from individual Co atoms and are not due to other types of surface defect.

NATURE PHYSICS ARTICLES

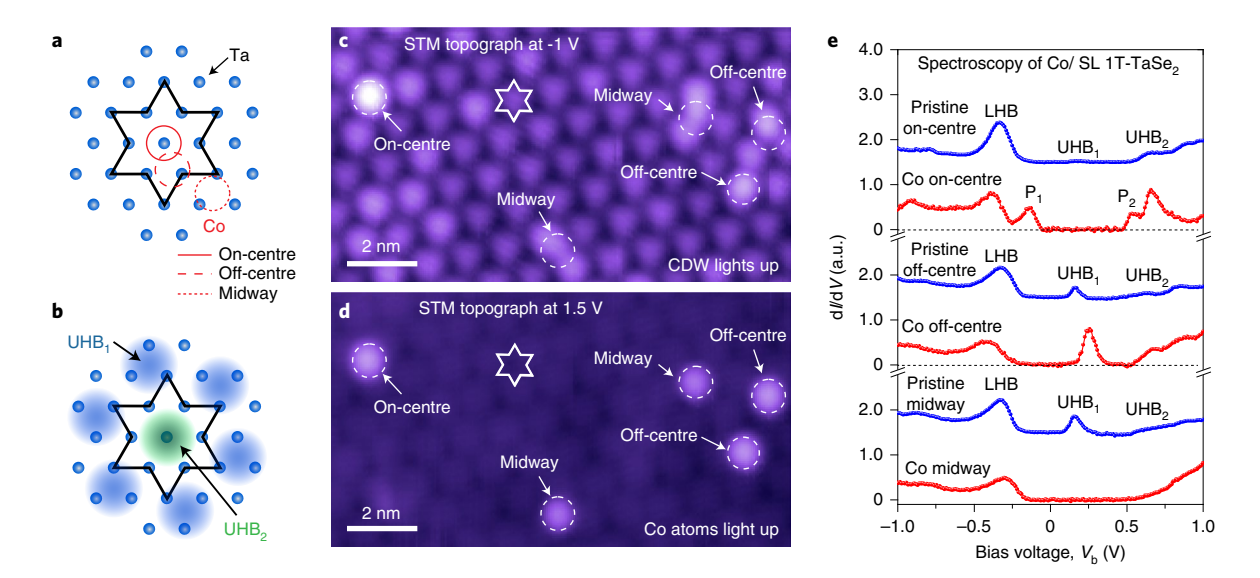


Fig. 2 | **Electronic behaviour of Co adatoms at different locations on SL 1T-TaSe₂. a**, Three possible locations for Co atoms in the SOD CDW unit cell for SL 1T-TaSe₂. **b**, Spatial distribution of LDOS in UHB₁ (blue) and UHB₂ (green) (from ref. ²³). The LHB LDOS coincides spatially with the UHB₂ LDOS. **c**, STM topograph taken at moderate negative sample bias, showing Co adatoms (dashed circles) and the SL 1T-TaSe₂ CDW lattice simultaneously ($I_1 = 5 \text{ pA}$). **d**, STM topographic taken in the same region as **c** at high positive sample bias showing Co adatom locations (dashed circles) without the CDW background ($I_1 = 5 \text{ pA}$). **e**, STM dl/dV spectra of Co adatoms located at on-centre, off-centre and midway positions (red curves) compared with pristine SL 1T-TaSe₂ spectra taken at similar positions (blue curves). New P₁ and P₂ resonance peaks at Hubbard band edges emerge only for Co adatoms at the on-centre position ($V_h = -1 \text{ V}$, $I_1 = 20 \text{ pA}$, $V_{cms} = 10 \text{ mV}$).

As a control measure, we performed these same types of measurements using a nonmagnetic impurity, Au. Au atoms were deposited onto SL 1T-TaSe₂ under the same general conditions that we used for depositing Co atoms. An STM topograph of a single Au atom on SL 1T-TaSe₂ can be seen in the inset to Fig. 3. Au atoms show a preference for binding at the centre of SOD clusters. Occasionally, Au atoms were found at other positions on the surface, but in those cases the atoms were unstable under STM spectroscopy conditions (the only stable position for Au atoms being the on-centre position). The results of STM dI/dV spectroscopy performed with the STM tip held over a Au atom in the on-centre position can be seen in Fig. 3 (red curve). The Au adatom spectrum shows no new resonances compared with the reference spectrum (blue curve, using the same tip) and notably does not show either the P₁ or the P₂ peak that was observed for Co adatoms. Features in the Au adatom spectrum corresponding to the pristine LHB and UHB, resonances can be seen, although the LHB feature appears to be shifted to slightly lower voltage for the on-Au spectrum ($V_b = -0.46 \,\mathrm{V}$) compared with the pristine SL 1T-TaSe₂ spectrum ($V_b = -0.31 \text{ V}$).

The appearance of two new resonances symmetrically aligned adjacent to the Hubbard band edges, as seen for Co atoms in the on-centre position, is an unusual type of defect behaviour. Inelastic tunnelling channels associated with impurity spin or vibrational excitations can induce dI/dV steps^{26,27} or replicate existing lower-energy elastic dI/dV peaks²⁸ but cannot create new dI/dV peaks. Impurity doping can induce polaronic states dressed by phonons or spins, but they occur at only one side of the gap and/or require a static magnetic background^{29,30} (which is not present here¹³). Impurities coupled to a CDW can produce a pair of bound states, but they are typically located at the CDW gap edges rather than the Hubbard band edges³¹. For conventional semiconductors, band-edge resonances do occur for shallow donor and acceptor impurities, but at only one band edge. Donor states reside below the conduction band edge while acceptor states reside above the valence band edge, but it is abnormal for a single type of defect to exhibit a resonance at both energies simultaneously. Defect behaviour in Mott insulators is more poorly understood than in conventional semiconductors,

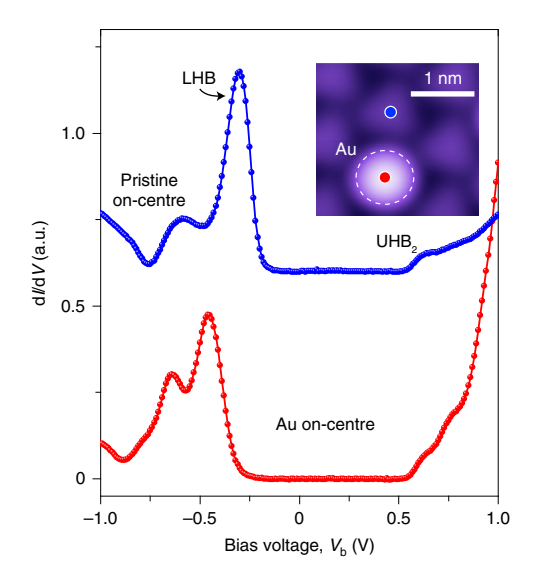


Fig. 3 | STM spectrum of a single nonmagnetic impurity (Au) on SL 1T-TaSe₂. STM dl/dV spectrum of a single Au adatom at the on-centre position on SL 1T-TaSe₂ (red curve) compared with a dl/dV spectrum of pristine SL 1T-TaSe₂ taken at the same position in the CDW lattice with the same STM tip (blue curve) (spectra obtained at colour-coded positions in the inset). No new resonance peaks at the Hubbard band edges are observed for on-centre Au ($V_b = -1 \text{V}$, $I_t = 50 \text{ pA}$, $V_{cm.s.} = 20 \text{ mV}$). Inset: STM topograph showing an on-centre Au adatom (dashed white circle) on SL 1T-TaSe₂ ($I_t = 5 \text{ pA}$, $V_b = -1 \text{ V}$).

but the behaviour we observe is unusual even for Mott insulators. In 'conventional' Mott insulators such as cuprates and iridates, for example, impurities have generally been found to induce broad in-gap states that fill up the Mott–Hubbard gap and metallize the system through a doping mechanism^{32–38}. In bulk 1T-TaS₂ (which has many similarities to SL 1T-TaSe₂), the Mott insulating state has

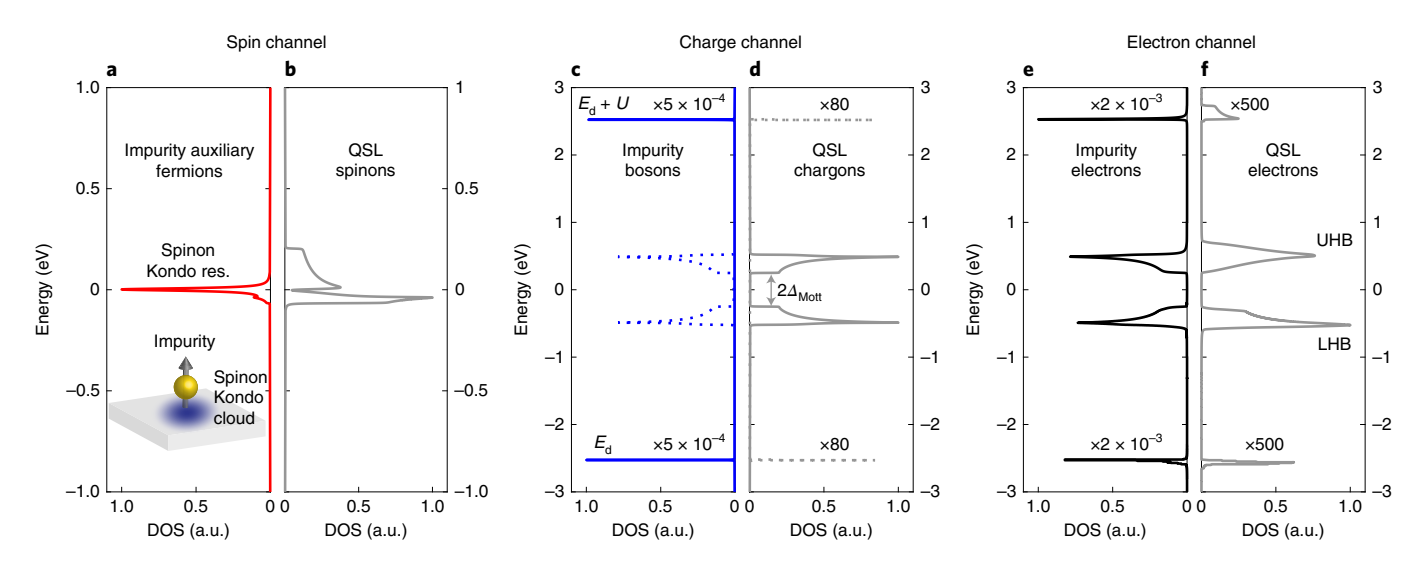


Fig. 4 | Calculated spinon Kondo effect. The Kondo effect for a magnetic impurity in contact with a QSL modelled using a modified Anderson model coupled to a U(1) QSL having a spinon Fermi surface. The model was solved using a slave-rotor mean-field technique whereby electrons are decomposed into auxiliary fermions and charged bosons (gauge fluctuations are ignored at this level). **a,b**, The resulting theoretical DOS spectra of impurity auxiliary fermions (**a**) and QSL auxiliary fermions ('spinons') (**b**) in the spin channel. Impurity auxiliary fermions show a sharp resonance at the Fermi level due to Kondo screening from itinerant QSL spinons. QSL spinon DOS shows a dip at E_F due to level repulsion from the Kondo resonance. Inset: Sketch representing the spinon Kondo screening cloud induced by a magnetic impurity in a QSL. **c,d**, Theoretical DOS spectra of impurity charged bosons (**c**) and QSL charged bosons ('chargons') (**d**) in the charge channel. In addition to its intrinsic bare impurity levels (' E_d ' and ' E_d + U'), the impurity charged boson inherits Hubbard band features (dashed curves) due to hybridization with QSL chargons. A similar effect occurs for the QSL chargons due to hybridization with the bare impurity levels. **e,f**, Theoretical total electron DOS spectra of the impurity (**e**) and QSL (**f**) obtained by convolving the spin and charge channels.

been shown to partially or fully collapse upon the introduction of defects or K adatoms, or the substitution of S with Se^{39–41}. The appearance of symmetrically placed resonances near the Hubbard band edges, however, has not previously been seen.

We are able to explain the observed behaviour of Co adatoms at the surface of 1T-TaSe, by the appearance of the Kondo effect for a magnetic impurity in contact with a gapless QSL. For the 'conventional' Fermi liquid Kondo effect, scattering between itinerant conduction electrons and a localized impurity spin leads to a many-body singlet state whose signature is a narrow 'Kondo resonance' at the Fermi level $(E_{\rm F})$. Such features have been observed by STM for individual magnetic impurities on metal surfaces and exhibit a Fano line shape in the electronic LDOS^{18,42}. For a gapless QSL the Kondo behaviour is predicted to be strikingly similar to the Fermi liquid case if one considers only the spin channel²⁰ (since spinons in a gapless QSL behave like the fermionic inhabitants of a 'neutral metal'). The problem lies in how to understand the experimental detection of a Kondo resonance that exists only in the spin channel of a Mott insulator. The solution is to take into account both the spin and charge channels simultaneously. Since conventional STMs can only tunnel electrons into a material, these electrons must decompose into both spinons and chargons once they are inside a QSL (since these are the elementary excitations of QSLs³). The STM electron tunnel current into a QSL can thus be expressed as a convolution of the spinon and chargon density of states 9,24,43,44. If one wants to use STM to detect a Kondo resonance in the spin channel of a QSL, one must therefore consider how it will appear when the spinon density of states is appropriately convoluted with the simultaneously occurring chargon density of states.

Such reasoning led us to calculate both the spinon and chargon density of states for a magnetic impurity in contact with a QSL. To accomplish this, we utilized a modified Anderson model incorporating a U(1) QSL exhibiting a spinon Fermi surface (the model parameters are mostly determined by experimental spectra; Methods, Supplementary Note 1 and ref. ⁴⁵). The model was solved using a slave-rotor mean-field theory where electrons are

decomposed into spin-1/2 auxiliary fermions (the spin channel) and charged spinless bosons (the charge channel)^{8,44,46}. The auxiliary fermions and charged bosons within the QSL (not including the impurity) are referred to as spinons and chargons, respectively. The solution of the Anderson model in the spin channel yields a Kondo resonance peak in the density of states (DOS) of the impurity auxiliary fermion at the Fermi level of the QSL spinon band (Fig. 4a). In the QSL spinon spectrum, the Kondo resonance manifests as a dip at the Fermi level (Fig. 4b), which can be rationalized as level repulsion in a standard Fano-type scenario (that is, involving a discrete state in resonance with a continuum)^{42,47}.

In the charge channel, the impurity charged boson hybridizes with QSL chargon states, resulting in an intermixing of their DOS spectra (Fig. 4c,d). For example, in addition to having the usual bare impurity levels (' $E_{\rm d}$ ' and ' $E_{\rm d}+U$ '), the impurity exhibits new spectral features that appear at the QSL Hubbard band energies (Fig. 4c, dashed lines) which are inherited from the QSL chargon spectrum. Similarly, the QSL chargon DOS spectrum exhibits weak peaks at $E_{\rm d}$ and $E_{\rm d}+U$ (Fig. 4d, dashed lines) that originate from the bare impurity levels.

To obtain the final predicted tunnelling DOS for electrons, the spin and charge channels must be combined via convolution (Methods and refs. 9,24,43,44) into a total electron channel. The result of this convolution can be seen in Fig. 4 for both the impurity (Fig. 4e) and the QSL continuum (Fig. 4f). The resulting impurity electronic DOS spectrum (Fig. 4e) exhibits a step function at the Hubbard band edges (that is, at the energies $\pm \Delta_{\text{Mott}}$) that is more abrupt than the linear dispersion seen in the absence of impurity (Supplementary Fig. 6c). However, there are no peaks at the band edges that resemble the experimental P_1 and P_2 features of Fig. 1d.

Explaining the experimentally observed side-peaks in the on-Co STS requires the incorporation of more realistic effects into our model, namely the inclusion of longitudinal gauge-field fluctuations (Methods, Supplementary Note 2 and ref. ⁴⁵). The reason for this is that, in a U(1) QSL with a spinon Fermi surface, both spinons and chargons couple to an emergent U(1) gauge field⁶. Since spinons

NATURE PHYSICS ARTICLES

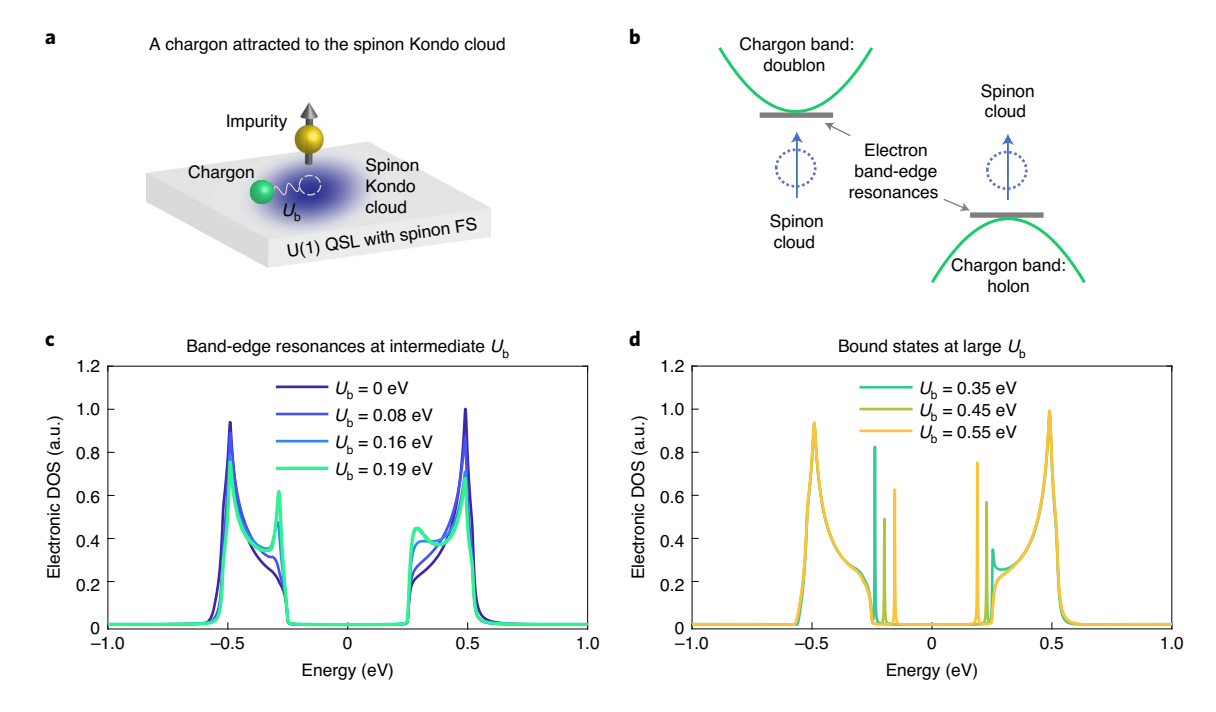


Fig. 5 | Gauge-field fluctuations induce electronic band-edge resonances and bound states. a, Sketch showing the inclusion of gauge-field fluctuations generating an effective attraction U_b that binds a QSL chargon to the spinon Kondo cloud. FS, Fermi surface. **b**, Energy diagram illustrating the formation of spinon-chargon band-edge resonance states due to the attraction between chargons and the spinon Kondo cloud. **c**, With increasing binding interaction U_b , the impurity electronic DOS spectrum exhibits growing resonance peaks at the Hubbard band edges. At $U_b = 0.19$ eV, the theoretical electronic resonances (green line) best reproduce the experimental observation in Fig. 1d. **d**, At even larger binding interaction U_b , the spinon-chargon states move inside the Mott gap and form very narrow bound states that do not match the experiment (an extrinsic broadening of 0.01 eV was applied in **d** to better visualize the bound-state peaks; Supplementary Note 2).

and chargons have opposite gauge charge 48,49 , the gauge field produces an effective binding interaction $U_{\rm b}$ (which is short ranged here owing to the screening of the gauge field by the spinon Fermi sea). Around a magnetic impurity, the localized spinon Kondo screening cloud therefore attracts chargons in both the holon and doublon branches (Fig. 5a), forming composite spinon–chargon states at energies both near the bottom of the doublon branch and near the top of the holon branch (Fig. 5b), in analogy to the donor and acceptor states of a semiconductor.

Inclusion of this gauge binding effect into our model causes a pile-up of spectral weight near the band edges of the impurity electronic DOS. The pile-up appears for small binding interaction $U_b = 0.08 \,\mathrm{eV}$ and increases smoothly with increasing U_b in the range shown in Fig. 5c. The value $U_b = 0.19 \,\mathrm{eV}$ results in a pair of resonance peaks at the Hubbard band edges of the impurity electronic DOS that best fits our data. The P₁ and P₂ side-peaks in our experimental STM spectrum (Fig. 1d) can thus be understood to reflect composite spinon-chargon states induced by the spinon Kondo cloud around a magnetic impurity, with peak widths determined by hybridization with QSL electrons. When U_b is increased beyond a critical value of ~0.35 eV (Fig. 5d and Supplementary Fig. 7), the band-edge resonances move inside the gap, forming narrow in-gap bound states that have no intrinsic width and require an extrinsic broadening to be better visualized (Supplementary Note 2). We find that varying model parameters such as the Coulomb repulsion, U, and hybridization, V, modifies the spinon Kondo temperature (T_{κ}) but does not qualitatively change the physical picture presented here. As long as the impurity is in the Kondo screening regime with $T < T_K$, then spin correlations will always induce band-edge resonance peaks at the site of the impurity when the gauge binding interaction, U_b , is sufficiently large. This mechanism also applies to impurities with spin higher than $s=\frac{1}{2}$ that could potentially be underscreened 50 by the Kondo effect. Our best-fit value of $U_{\rm b}$

(0.19 eV) additionally agrees with the theoretical estimate that U_b is about half of the spinon band width⁴⁵. This interaction strength is sufficient to induce pronounced band-edge resonance peaks in the spectrum of a magnetic impurity on the QSL, but for a pristine QSL, it merely shifts the positions of the LHB and UHB peaks (Supplementary Fig. 6).

Our observed Co adatom position dependence in the CDW unit cell is consistent with the orbital nature of the 1T-TaSe, Hubbard bands in this overall scenario. Because the SOD unit cell is composed of 13 Ta atoms (each containing one d electron²³), the fundamental building block of the SL 1T-TaSe, Mott bands is more akin to a molecular orbital than to an individual atomic state. This is manifest, for example, in the position dependence of UHB₁ for the pristine material (which is stronger away from the SOD centre) and in UHB₂ (which is stronger near the SOD centre) (Fig. 2b). Our calculations do not include this level of orbital complexity, but the experimental appearance of a strong Kondo effect involving UHB₂ for Co in the on-centre position is qualitatively consistent with this reasoning. When a Co adatom is moved away from the on-centre position, we expect coupling between the impurity and the QSL charge distribution to reduce, thus reducing the Kondo temperature below our detection limits (Supplementary Figs. 8 and 9). Similar reasoning could explain why impurity coupling to UHB, does not result in a detectable Kondo effect. The placement of nonmagnetic atoms (such as Au) onto the on-centre position is similarly not expected to result in Kondo-induced resonance peaks due to the lack of spin-based exchange coupling, consistent with the experimental data (Fig. 3).

In conclusion, we deposited isolated magnetic adatoms onto the single-layer QSL candidate 1T-TaSe₂. Magnetic impurities having large hybridization with the underlying Hubbard band LDOS develop a pair of resonance peaks at the Hubbard band edges, consistent with the impurity electronic DOS obtained from a modified

Anderson model incorporating a U(1) gapless QSL. This provides evidence supporting the existence of a spinon-based Kondo effect in a gapless QSL. Future experiments that more directly probe the magnetic moments of impurities could provide further insight into spinon-induced Kondo screening²². Our ability to perform atomically precise impurity manipulation and spectroscopy with the STM tip might be applied to other layered QSL systems to gain microscopic control over other exotic excitations such as non-abelian anyons^{51–54}.

Online content

Any methods, additional references, Nature Research reporting summaries, source data, extended data, supplementary information, acknowledgements, peer review information; details of author contributions and competing interests; and statements of data and code availability are available at https://doi.org/10.1038/s41567-022-01751-4.

Received: 14 September 2021; Accepted: 8 August 2022; Published online: 29 September 2022

References

- Zhou, Y., Kanoda, K. & Ng, T.-K. Quantum spin liquid states. Rev. Mod. Phys. 89, 025003 (2017).
- 2. Balents, L. Spin liquids in frustrated magnets. Nature 464, 199-208 (2010).
- Lee, P. A., Nagaosa, N. & Wen, X.-G. Doping a Mott insulator: physics of high-temperature superconductivity. Rev. Mod. Phys. 78, 17–85 (2006).
- Savary, L. & Balents, L. Quantum spin liquids: a review. Rep. Prog. Phys. 80, 016502 (2016).
- 5. Motrunich, O. I. Variational study of triangular lattice spin-1/2 model with ring exchanges and spin liquid state in κ -(ET)₂Cu₂(CN)₃. *Phys. Rev. B* **72**, 045105 (2005).
- Block, M. S., Sheng, D. N., Motrunich, O. I. & Fisher, M. P. A. Spin Bose-metal and valence bond solid phases in a spin-1/2 model with ring exchanges on a four-leg triangular ladder. *Phys. Rev. Lett.* 106, 157202 (2011).
- He, W.-Y., Xu, X. Y., Chen, G., Law, K. T. & Lee, P. A. Spinon Fermi surface in a cluster Mott insulator model on a triangular lattice and possible application to 1T-TaS₂, *Phys. Rev. Lett.* 121, 046401 (2018).
- 8. Lee, S.-S. & Lee, P. A. U(1) gauge theory of the Hubbard model: spin liquid states and possible application to κ -(BEDT-TTF)₂Cu₂(CN)₃. *Phys. Rev. Lett.* **95**, 036403 (2005).
- 9. Mross, D. F. & Senthil, T. Charge Friedel oscillations in a Mott insulator. *Phys. Rev. B* **84**, 041102 (2011).
- Yamashita, M. et al. Highly mobile gapless excitations in a two-dimensional candidate quantum spin liquid. Science 328, 1246–1248 (2010).
- Shen, Y. et al. Evidence for a spinon Fermi surface in a triangular-lattice quantum-spin-liquid candidate. Nature 540, 559–562 (2016).
- Paddison, J. A. M. et al. Continuous excitations of the triangular-lattice quantum spin liquid YbMgGaO₄. Nat. Phys. 13, 117–122 (2017).
- 13. Klanjšek, M. et al. A high-temperature quantum spin liquid with polaron spins. *Nat. Phys.* **13**, 1130–1134 (2017).
- Yamashita, M. Boundary-limited and glassy-like phonon thermal conduction in EtMe₃Sb[Pd(dmit)₂]₂. J. Phys. Soc. Jpn. 88, 083702 (2019).
- 15. Bourgeois-Hope, P. et al. Thermal conductivity of the quantum spin liquid candidate EtMe₃Sb[Pd(dmit)₂]₂: no evidence of mobile gapless excitations. *Phys. Rev. X* **9**, 041051 (2019).
- 16. Ni, J. M. et al. Absence of magnetic thermal conductivity in the quantum spin liquid candidate EtMe₃Sb[Pd(dmit)₂]₂. *Phys. Rev. Lett.* **123**, 247204 (2019).
- Zhu, Z., Maksimov, P. A., White, S. R. & Chernyshev, A. L. Disorder-induced mimicry of a spin liquid in YbMgGaO₄. Phys. Rev. Lett. 119, 157201 (2017).
- Madhavan, V., Chen, W., Jamneala, T., Crommie, M. F. & Wingreen, N. S. Tunneling into a single magnetic atom: spectroscopic evidence of the Kondo resonance. Science 280, 567–569 (1998).
- 19. Hudson, E. W. et al. Interplay of magnetism and high- T_c superconductivity at individual Ni impurity atoms in Bi₂Sr₂CaCu₂O_{8+ δ}. Nature **411**, 920–924 (2001).
- 20. Ribeiro, P. & Lee, P. A. Magnetic impurity in a U(1) spin liquid with a spinon Fermi surface. *Phys. Rev. B* **83**, 235119 (2011).
- Hewson, A. C. The Kondo Problem to Heavy Fermions (Cambridge Univ. Press, 1993).
- Gomilšek, M. et al. Kondo screening in a charge-insulating spinon metal. Nat. Phys. 15, 754–758 (2019).
- Chen, Y. et al. Strong correlations and orbital texture in single-layer 1T-TaSe₂. Nat. Phys. 16, 218–224 (2020).
- Ruan, W. et al. Evidence for quantum spin liquid behaviour in singlelayer 1T-TaSe₂ from scanning tunnelling microscopy. *Nat. Phys.* 17, 1154–1161 (2021).

 Ge, Y. & Liu, A. Y. First-principles investigation of the charge-density-wave instability in 1T-TaSe₂. Phys. Rev. B 82, 155133 (2010).

- Heinrich, A. J., Gupta, J. A., Lutz, C. P. & Eigler, D. M. Single-atom spin-flip spectroscopy. Science 306, 466–469 (2004).
- Hirjibehedin, C. F., Lutz, C. P. & Heinrich, A. J. Spin coupling in engineered atomic structures. Science 312, 1021–1024 (2006).
- Garnier, L. et al. The Kondo effect of a molecular tip as a magnetic sensor. Nano Lett. 20, 8193–8199 (2020).
- Franchini, C., Reticcioli, M., Setvin, M. & Diebold, U. Polarons in materials. Nat. Rev. Mater. 6, 560–586 (2021).
- Setvin, M. et al. Direct view at excess electrons in TiO₂ rutile and anatase. Phys. Rev. Lett. 113, 086402 (2014).
- Tütto, I. & Zawadowski, A. Quantum theory of local perturbation of the charge-density wave by an impurity: Friedel oscillations. *Phys. Rev. B* 32, 2449–2470 (1985).
- Cai, P. et al. Visualizing the evolution from the Mott insulator to a charge-ordered insulator in lightly doped cuprates. *Nat. Phys.* 12, 1047–1051 (2016).
- Ye, C. et al. Visualizing the atomic-scale electronic structure of the Ca₂CuO₂Cl₂ Mott insulator. Nat. Commun. 4, 1365 (2013).
- Okada, Y. et al. Imaging the evolution of metallic states in a correlated iridate. Nat. Mater. 12, 707–713 (2013).
- Battisti, I. et al. Universality of pseudogap and emergent order in lightly doped Mott insulators. Nat. Phys. 13, 21–25 (2017).
- Zhao, H. et al. Atomic-scale fragmentation and collapse of antiferromagnetic order in a doped Mott insulator. Nat. Phys. 15, 1267–1272 (2019).
- Yan, Y. J. et al. Electron-doped Sr₂IrO₄: an analogue of hole-doped cuprate superconductors demonstrated by scanning tunneling microscopy. *Phys. Rev.* X 5, 041018 (2015).
- 38. Sun, Z. et al. Evidence for a percolative Mott insulator-metal transition in doped Sr,IrO₄. *Phys. Rev. Res.* **3**, 023075 (2021).
- Cho, D., Cho, Y.-H., Cheong, S.-W., Kim, K.-S. & Yeom, H. W. Interplay of electron–electron and electron–phonon interactions in the low-temperature phase of 1T–TaS₂. *Phys. Rev. B* **92**, 293602 (2015).
- Zhu, X.-Y. et al. Realization of a metallic state in 1T-TaS₂ with persisting long-range order of a charge density wave. *Phys. Rev. Lett.* 123, 206405 (2019).
- Qiao, S. et al. Mottness collapse in 1T—TaS_{2-x}Se_x transition-metal dichalcogenide: an interplay between localized and itinerant orbitals. *Phys. Rev. X* 7, 041054 (2017).
- Madhavan, V., Chen, W., Jamneala, T., Crommie, M. F. & Wingreen, N. S. Local spectroscopy of a Kondo impurity: Co on Au(111). *Phys. Rev. B* 64, 165412 (2001).
- Kim, B. J. et al. Distinct spinon and holon dispersions in photoemission spectral functions from one-dimensional SrCuO₂. Nat. Phys. 2, 397–401 (2006).
- 44. Florens, S. & Georges, A. Quantum impurity solvers using a slave rotor representation. *Phys. Rev. B* **66**, 165111 (2002).
- 45. He, W.-Y. & Lee, P. A. Magnetic impurity as a local probe of the U(1) quantum spin liquid with spinon Fermi surface. *Phys. Rev. B* **105**, 195156
- Florens, S. & Georges, A. Slave-rotor mean-field theories of strongly correlated systems and the Mott transition in finite dimensions. *Phys. Rev. B* 70, 035114 (2004).
- Fano, U. Effects of configuration interaction on intensities and phase shifts. *Phys. Rev.* 124, 1866–1878 (1961).
- Wen, X.-G. & Lee, P. A. Theory of underdoped cuprates. Phys. Rev. Lett. 76, 503–506 (1996).
- Lee, P. A., Nagaosa, N., Ng, T.-K. & Wen, X.-G. SU(2) formulation of the t-J model: application to underdoped cuprates. *Phys. Rev. B* 57, 6003–6021 (1998).
- 50. Nagaosa, N. Quantum Field Theory in Strongly Correlated Electronic Systems (Springer, 1999).
- Dhochak, K., Shankar, R. & Tripathi, V. Magnetic impurities in the honeycomb Kitaev model. *Phys. Rev. Lett.* 105, 117201 (2010).
- Vojta, M., Mitchell, A. K. & Zschocke, F. Kondo impurities in the Kitaev spin liquid: numerical renormalization group solution and gauge-flux-driven screening. *Phys. Rev. Lett.* 117, 037202 (2016).
- 53. Banerjee, A. et al. Neutron scattering in the proximate quantum spin liquid α -RuCl₃. Science **356**, 1055–1059 (2017).
- Janša, N. et al. Observation of two types of fractional excitation in the Kitaev honeycomb magnet. Nat. Phys. 14, 786–790 (2018).

Publisher's note Springer Nature remains neutral with regard to jurisdictional claims in published maps and institutional affiliations.

Springer Nature or its licensor holds exclusive rights to this article under a publishing agreement with the author(s) or other rightsholder(s); author self-archiving of the accepted manuscript version of this article is solely governed by the terms of such publishing agreement and applicable law.

© The Author(s), under exclusive licence to Springer Nature Limited 2022

NATURE PHYSICS ARTICLES

Methods

Sample growth. Single-layer 1T-TaSe $_2$ films were grown on epitaxial bilayer graphene-terminated 6H-SiC(0001) substrates in a molecular beam epitaxy chamber operating at ultrahigh vacuum (base pressure 2×10^{-10} Torr) at the HERS endstation of Beamline 10.0.1, Advanced Light Source, Lawrence Berkeley National Laboratory. High-purity Ta (99.9%) and Se (99.999%) were evaporated from an electron beam evaporator and a standard Knudsen cell, respectively, with a Ta:Se flux ratio set between 1:10 and 1:20 and a substrate temperature of 660 °C. The growth process was monitored by reflection high-energy electron diffraction. Before taking the films out of vacuum for STM/STS measurements, Se capping layers with ~10 nm thickness were deposited onto the samples for passivation. These were later removed by ultrahigh-vacuum annealing at ~180 °C for 1 h.

STM/STS measurements. STM/STS measurements were performed using a commercial CreaTec STM/AFM system at $T=5\,\mathrm{K}$ under ultrahigh-vacuum conditions. To avoid tip artefacts, STM tips were calibrated on a Au(111) surface by measuring its herringbone surface reconstruction and Shockley surface state before all STM/STS measurements. STS dI/dV spectra were obtained using standard lock-in techniques with a small bias modulation at 401 Hz. High-purity Co wire (99.99%) was used to evaporate Co atoms from an electron beam evaporator onto cold samples kept in the STM head (to avoid adatom clustering). Co evaporation was first calibrated on Au(111) substrates where the existence of isolated Co atoms was confirmed through their known Kondo resonance features [8,42]. Single-layer 1T-TaSe₂/bilayer graphene on SiC was then transferred into the STM and brought to thermal equilibrium before performing another Co evaporation using identical deposition parameters. High-purity Au wire (99.99%) was used to evaporate Au atoms via direct heating onto cold samples kept in the STM head (that is, by wrapping the Au wire around a W filament heater).

Anderson impurity model on QSL. The following Hamiltonian was used to describe an atomic impurity with on-site repulsion *U* embedded in a QSL:

$$H = \sum_{\sigma} E_d d_{\sigma}^{\dagger} d_{\sigma} + U d_{\uparrow}^{\dagger} d_{\uparrow} d_{\downarrow}^{\dagger} d_{\downarrow} + V \sum_{\sigma} \left(c_{\sigma,\mathbf{R}}^{\dagger} d_{\sigma} + d_{\sigma}^{\dagger} c_{\sigma,\mathbf{R}} \right) + H_{\mathrm{h}}.$$

Here E_d is the on-site energy, $\sigma=\uparrow/\downarrow$ is the spin index, V is the coupling between the impurity and the QSL electronic state at the nearest-neighbour site ${\bf R}$ and $H_{\rm h}=t\sum_{{\bf r},{\bf r}',\sigma}c^{\dagger}_{{\bf r},\sigma}c_{{\bf r}',\sigma}+U_{\rm QSL}\sum_{{\bf r}}c^{\dagger}_{{\bf r},\uparrow}c_{{\bf r},\uparrow}c^{\dagger}_{{\bf r},\downarrow}c_{{\bf r},\downarrow}$ is the half-filled Hubbard model for the QSL. The electronic annihilation (creation) operators of the impurity and the QSL are denoted by $d^{(\dagger)}_{\sigma}$ and $c^{(\dagger)}_{\sigma}$, respectively.

The half-filled Hubbard model for the QSL has a slave-rotor mean-field solution, which fractionalizes the electrons in the QSL as $c_{\sigma,\mathbf{r}}^{\dagger} = f_{\sigma,\mathbf{r}}^{\dagger} X_{\mathbf{r}}$ and $c_{\sigma,\mathbf{r}} = f_{\sigma,\mathbf{r}} X_{\mathbf{r}}^{\dagger}$, with $f_{\sigma,\mathbf{r}}^{\dagger}$ and $X_{\mathbf{r}}^{(\dagger)}$ being the annihilation (creation) operators of the spinons and chargons, respectively. The spinon and chargon band dispersions in the OSL are taken to be

$$\begin{split} \xi_{\mathbf{k}} &= 2t_{\mathrm{f}} \left(2 \mathrm{cos} \frac{1}{2} k_x a \mathrm{cos} \frac{\sqrt{3}}{2} k_y a + \mathrm{cos} k_x a \right) - \mu_{\mathrm{f}}, \\ \varepsilon_{\mathbf{k}} &= 2t_{\mathrm{X}} \left(2 \mathrm{cos} \frac{1}{2} k_x a \mathrm{cos} \frac{\sqrt{3}}{2} k_y a + \mathrm{cos} k_x a - 3 \right) + \Delta_{\mathrm{Mott}}, \end{split}$$

where (k_x, k_y) denotes the quasimomentum of the Bloch states in a triangular lattice and a is the lattice constant. Here $\Delta_{\text{Most}} = 0.25 \,\text{eV}$ is fixed by the experimentally observed Mott gap size (which coincides with $U_{\text{QSI}}/2$ in the atomic limit). The hopping parameters $t_i = 0.03 \,\text{eV}$ and $t_{\text{X}} = -0.03 \,\text{eV}$ are determined by the experimentally observed band width of pristine SL 1T-TaSe₂, while the half-filling requirement of the spinon band fixes the chemical potential to be $\mu_i = -0.024 \,\text{eV}$.

In the slave-rotor mean-field formalism, the electron operators of the impurity are rewritten as $d_\sigma^\dagger=a_\sigma^\dagger X_d$, $d_\sigma=a_\sigma X_d^\dagger$. For the impurity electron, $a_\sigma^{(\dagger)}$ annihilates (creates) a spin-1/2 auxiliary fermion that represents the spin degree of freedom of the impurity electron and $X_d^{(\dagger)}$ annihilates (creates) a spinless charged boson that corresponds to its charge degree of freedom. The coupling between the Anderson impurity and the QSL was solved using the slave-rotor mean field so that the Green's functions for the spin-1/2 auxiliary fermion and the charged boson at the impurity could be obtained. Here, the bare Co Coulomb energy U and the hopping V between the Co atom and the QSL are taken to be $U=5\,\mathrm{eV}$ and $V=0.23\,\mathrm{eV}$, which yield a Kondo temperature of $T_K=19\,\mathrm{K}$. Variation of U and V changes the Kondo temperature but does not significantly affect our main results (that is, the appearance of band-edge resonance peaks in the Kondo regime with $T< T_K$). More details regarding the Green's function constructed from the slave-rotor mean-field theory can be found in Supplementary Note 1 and ref. 45 .

Spectral function calculations. The electronic spectral function (that is, the LDOS) at the impurity and the QSL is the imaginary part of the retarded Green's function. For the impurity electron, the thermal Green's function is given by the correlation function

$$\begin{split} &G_{d,\sigma}^{0}\left(\mathrm{i}\omega_{n}\right)=-\left\langle d_{\sigma}\left(\mathrm{i}\omega_{n}\right)d_{\sigma}^{\dagger}\left(\mathrm{i}\omega_{n}\right)\right\rangle _{0}\\ &=-\frac{1}{\beta}\sum_{\nu_{+}}\left\langle a_{\sigma}\left(\mathrm{i}\omega_{n}+\mathrm{i}\nu_{n}\right)a_{\sigma}^{\dagger}\left(\mathrm{i}\omega_{n}+\mathrm{i}\nu_{n}\right)\right\rangle _{0}\left\langle X_{d}\left(\mathrm{i}\nu_{n}\right)X_{d}^{\dagger}\left(\mathrm{i}\nu_{n}\right)\right\rangle _{0}. \end{split}$$

Similarly, the thermal Green's function for the QSL electron at R is

$$\begin{split} &G_{c,\sigma}^{0}\left(\mathrm{i}\omega_{n},\mathbf{R},\mathbf{R}\right)=-\left\langle c_{\sigma}\left(\mathrm{i}\omega_{n}\right)c_{\sigma}^{\dagger}\left(\mathrm{i}\omega_{n}\right)\right\rangle _{0}\\ &=-\frac{1}{\beta}\sum_{\nu_{\nu}}\left\langle f_{\sigma,\mathbf{R}}\left(\mathrm{i}\omega_{n}+\mathrm{i}\nu_{n}\right)f_{\sigma,\mathbf{R}}^{\dagger}\left(\mathrm{i}\omega_{n}+\mathrm{i}\nu_{n}\right)\right\rangle _{0}\left\langle X_{\mathbf{R}}\left(\mathrm{i}\nu_{n}\right)X_{\mathbf{R}}^{\dagger}\left(\mathrm{i}\nu_{n}\right)\right\rangle _{0}. \end{split}$$

Here, ω_n and ν_n are the fermionic and bosonic Matsubara frequencies, respectively, and $\langle \cdots \rangle_0$ means the thermal average calculated through the Anderson impurity Hamiltonian H. Analytic continuation $i\omega_n \to \omega + i0^+$ yields the corresponding retarded Green's function. The impurity electronic DOS shown in Fig. 4e and the QSL electronic DOS shown in Fig. 4f are given by $-\frac{1}{\pi} {\rm Im} G^0_{d,\sigma} \left(\omega\right)$ and $-\frac{1}{\pi} {\rm Im} G^0_{d,\sigma} \left(\omega\right)$, respectively. The detailed forms of these correlation functions are given in Supplementary Note 1.

Chargons and spinons in the QSL carry opposite gauge charge, and so longitudinal gauge fluctuations yield an effective binding between them⁴⁹:

$$U_{\rm b} \sum_{\sigma} f_{\sigma,\mathbf{R}}^{\dagger} f_{\sigma,\mathbf{R}} \left(a_{\mathbf{R}}^{\dagger} a_{\mathbf{R}} - b_{\mathbf{R}}^{\dagger} b_{\mathbf{R}} \right)$$

with $a_{\mathbf{R}}^{(\dagger)}$ and $b_{\mathbf{R}}^{(\dagger)}$ being the holon and doublon annihilation (creation) operators, respectively, which together compose the chargon creation and annihilation operators, $X_{\mathbf{R}}^{\dagger} = a_{\mathbf{R}} + b_{\mathbf{R}}^{\dagger}$ and $X_{\mathbf{R}} = a_{\mathbf{R}}^{\dagger} + b_{\mathbf{R}}$. Incorporating the spinon–chargon binding interaction into the Anderson impurity Hamiltonian results in a modified correlation function that yields the final impurity electron thermal Green's function:

$$G_{d,\sigma}\left(\mathrm{i}\omega_{n}\right)=-\left\langle d_{\sigma}\left(\mathrm{i}\omega_{n}\right)d_{\sigma}^{\dagger}\left(\mathrm{i}\omega_{n}\right)
ight
angle .$$

The impurity DOS spectrum is given by $-\frac{1}{\pi} \text{Im} G_{d,\sigma} \left(i\omega_n \to \omega + i0^+ \right)$ and exhibits a pair of resonance peaks at the Hubbard band edges as shown in Fig. 5. The detailed form of $G_{d,\sigma} \left(i\omega_n \right)$ can be found in Supplementary Note 2.

DFT simulation of Co on single-layer 1T-TaSe₂. First-principles calculations of Co on the CDW phase of single-layer 1T-TaSe2 were performed using DFT as implemented in the Quantum ESPRESSO package. A slab model with a 16 Å vacuum layer was adopted to avoid interactions between periodic images. We employed optimized norm-conserving Vanderbilt pseudopotentials including Ta 5s and 5p semicore states (with a plane-wave energy cut-off of 90 Ry) as well as the Perdew-Burke-Ernzerhof exchange-correlation functional in the generalized gradient approximation. Every CDW unit cell was assumed to host a Co atom above its central Ta atom, and the structure was fully relaxed at the DFT Perdew-Burke-Ernzerhof level until the force on each atom was less than 0.02 eV Å-1. On-site Hubbard interactions were added through the simplified rotationally invariant approach using $U=2\,\mathrm{eV}$ for each Ta atom and $U=3\,\mathrm{eV}$ for each Co 6. DFT simulation results show that the Co atom on single-layer 1T-TaSe, slightly *n*-dopes the system and hosts a magnetic moment of 1.86 μ_B , where μ_B is the Bohr magneton. The spin density associated with Co on single-layer 1T-TaSe, is shown in Supplementary Fig. 1.

Data availability

The data represented in Figs. 1d, 2e, 3, 4 and 5 are available as Source Data files. All other data that support the plots within this paper and other findings of this study are available upon request. Source data are provided with this paper.

Code availability

The codes used in the calculations shown in Figs. 4, 5c, 5d, 86a-c, 86d, 87, 88 and 89 are available as Supplementary Data Files 1-8.

References

- Wang, L., Maxisch, T. & Ceder, G. Oxidation energies of transition metal oxides within the GGA+U framework. *Phys. Rev. B* 73, 195107 (2006).
- 56. de la Peña O'Shea, V. A., Moreira, I. D. P. Ř., Roldán, A. & Illas, F. Electronic and magnetic structure of bulk cobalt: the α , β , and ϵ -phases from density functional theory calculations. *J. Chem. Phys.* **133**, 024701 (2010).

Acknowledgements

This research was supported by the US Department of Energy, Office of Science, National Quantum Information Science Research Centers, Quantum Systems Accelerator (STM/STS measurements) and the Advanced Light Source (sample growth) funded by the Director, Office of Science, Office of Basic Energy Sciences, Materials Sciences and Engineering Division, of the US Department of Energy under contract no. DE-AC02-05CH1231. Support was also provided by National Science Foundation awards DMR-2221750 (topographic characterization) and DMR-1926004 (DFT calculations). The work at the Stanford Institute for Materials and Energy Sciences and Stanford University (surface treatment) was supported by the DOE Office of Basic Energy Sciences, Division of Material Science. P.A.L. acknowledges support from DOE Basic Energy Science award number DE-FG02-03ER46076 (theoretical QSL analysis). H.R. acknowledges support from a National Research Foundation of Korea grant funded by the government of

Korea (MSIT) (no. 2021R1A2C2014179) (growth characterization). W.R. acknowledges fellowship support from Shanghai Science and Technology Development Funds (no. 22QA1400600).

Author contributions

Y.C., W.R., P.A.L. and M.F.C. initiated and conceived this project. Y.C., W.R., R.L.L., T.Z. and C.Z. carried out STM/STS measurements under the supervision of M.F.C. J.H., S.T. and H.R. performed sample growth under the supervision of Z.-X.S. and S.-K.M. W.Y.H. performed slave-rotor calculations and theoretical analysis under the supervision of P.A.L. M.W. performed DFT calculations under the supervision of S.G.L. Y.C., W.Y.H., W.R., P.A.L. and M.F.C. wrote the manuscript with the help from all authors. All authors contributed to the scientific discussion.

Competing interests

The authors declare no competing interests.

Additional information

 $\label{thm:continuous} \textbf{Supplementary information} \ The online version contains supplementary material available at <math display="block"> https://doi.org/10.1038/s41567-022-01751-4.$

Correspondence and requests for materials should be addressed to Michael F. Crommie.

Peer review information *Nature Physics* thanks Elio Koenig and the other, anonymous, reviewer(s) for their contribution to the peer review of this work.

Reprints and permissions information is available at www.nature.com/reprints.